

The 2003 Bam (Iran) earthquake – rupture of a blind strike-slip fault: auxiliary material

Morteza Talebian,¹ Eric J. Fielding,^{2,3} Gareth J. Funning,⁴

Manoucher Ghorashi,¹ James Jackson,² Hamid Nazari,¹ Barry Parsons,⁴

Keith Priestley,² Paul A. Rosen,³ Richard Walker,² and Tim J. Wright⁴.

M. Talebian, M. Ghorashi, H. Nazari, Geological Survey of Iran, PO Box 13185-1494, Tehran, Iran

E. J. Fielding, P. A. Rosen, Jet Propulsion Laboratory, California Institute of Technology, Pasadena, California, USA

G. J. Funning, B. Parsons, T. J. Wright, Centre for the Observation and Modelling of Earthquakes and Tectonics, Dept of Earth Sciences, Parks Road, Oxford, OX1 3PR, UK (gareth.funning@earth.ox.ac.uk)

J. A. Jackson, K. Priestley, R. Walker, Centre for the Observation and Modelling of Earthquakes and Tectonics, Bullard Laboratories, Madingley Rise, Madingley Road, Cambridge, CB2 0EZ, UK.

¹Geological Survey of Iran, PO Box 13185-1494, Tehran, Iran.

²COMET, Department of Earth Sciences, University of Cambridge, U.K.

³Jet Propulsion Laboratory, California Institute of Technology, U.S.A.

⁴COMET, Department of Earth Sciences, University of Oxford, U.K.

1. Improvement of effective baselines by combining interferograms

Topographic corrections for our interferograms were calculated using a digital elevation model (DEM) constructed from an ERS tandem pair of SAR images with a perpendicular baseline of -129 m, and calibrated with the SRTM30 global topographic dataset to remove long-wavelength tilts and warps. One drawback of using such a DEM is the possibility of incorporating atmospheric noise in the topographic signal. As the baseline of the coseismic pair of images for the Bam earthquake was over four times larger than that of the tandem pair used to generate the DEM (Table 1), this meant that the effects of any atmospheric noise present in the DEM would be carried over into the ‘corrected’ coseismic interferogram, and amplified by the ratio of baselines.

To improve the baseline of the coseismic interferogram, and therefore mitigate this effect, we use the result of Massonnet and Feigl [1998] whereby the difference image of two interferometric pairs is shown to have an effective baseline equal to the difference of the two baselines of the two pairs. A preseismic interferogram (Table 1), corrected for topography using our tandem pair DEM, and with a perpendicular baseline of ~ 450 m, was subtracted from the ~ 570 m-baseline coseismic interferogram (Table 1), also corrected with our DEM. The resulting differenced interferogram had an effective baseline of ~ 120 m, smaller than the baseline of the tandem pair, and contained an appreciably reduced component of noise due to atmospheric errors in the DEM when compared with the undifferenced coseismic interferogram. This method differs from the traditional ‘three-pass’ method of interferometry, as both interferograms were corrected

for topography using the same external DEM, and the subtracted pre-seismic image was not scaled by the ratio of the two baselines of the interferograms.

2. Interferometric correlation.

The interferograms were processed from the Level 1 (single-look complex) products using the ROI-PAC software [*Rosen et al.*, 2004] with 1 range and 5 azimuth looks to produce ~ 20 m pixels. The interferometric coherence was enhanced by the use of a spectral shift filter that compensates for the long spatial baseline of the pairs. The correlation shown in Figure 4 was calculated directly [equation 57 *Rosen et al.*, 2000]) from each SAR cell of this full-resolution interferogram to precisely locate the decorrelation due to the surface ruptures. A 2-D gaussian filter with a total (6σ) width of 200 m (full width at half maximum of 90 m) was applied to smooth the data for Figure 4 [*Wessel and Smith*, 1998]. The correlation in Figure 3c was calculated with a weighted averaging scheme over 3×3 pixels that is somewhat affected by high phase gradients causing lower correlation values. The 56 mm (C-band) wavelength of the Envisat radar means that the correlation is sensitive to objects that are 10 mm across and larger. The rest of the interferometric processing was performed after averaging the full-resolution interferogram by a further 4×4 looks to produce ~ 80 m pixels.

3. Seismic source mechanisms through body-wave modeling.

To compare synthetic and observed seismograms, all P wave seismograms are aligned at their short-period first-arrival times. Synthetics were calculated using the MT5 version [*Zwicky et al.*, 1994] of the algorithm of McCaffrey & Abers [1988] and McCaffrey *et al.* [1991]. The first motions of P and SH constrain the nodal plane orientations, particularly

the rake, quite tightly. However, we find that a single source solution (Auxiliary Figure 1) cannot match the seismograms in the west, because of a second upward pulse about 10 seconds after the onset in the north-west (e.g. at MTE, AQU) and a downward pulse at about 13 secs in the south-west (e.g. TSUM, LSZ). This second pulse cannot be pP (which would be down in the NW and up in the SE) and needs to be produced by a second source that does not greatly affect the already good fits to P waves in the east and SH at most azimuths.

A second source that is a N-S striking thrust achieves this (Auxiliary Figures 2–3). Here P waves are relatively big, in spite of the small moment, because of sP. SH is small everywhere, and stations in the west have a bigger P wave signal than those in the east, because of the dip (30°). The second source has an onset 9.5 seconds after the first, and is displaced south by 12 km. The fit is not good everywhere, particularly at stations near nodal planes (e.g. P at KBS and SH at TSUM), but for these it is rarely possible to fit all the detail, and it is more important that the amplitude remains small. The source parameters of the second pulse are not well resolved, and several trade-offs are possible, particularly between moment, source time function and depth. The moment is uncertain by at least 30%.

4. InSAR data reduction and elastic dislocation modeling.

The range change information within the SAR interferogram can be converted directly to displacement by unwrapping the interferometric phase and applying the relation that a range decrease of 2π is equivalent to a motion of the ground of half of a radar wavelength (~ 2.8 cm) towards the satellite, resolved into the satellite line-of-sight. The high degree

of spatial correlation of the displacement information in the interferogram allows us to resample these data to a lower resolution in order to expedite the inversion process. We employ a zoned sampling scheme, where the sample spacing used depends on the distance from the centre of deformation (400 m spacing within 7 km, 1 km spacing within 15 km, 5 km elsewhere). In this way we reduce the number of data points to be modeled from $\sim 10^6$ to ~ 2000 .

We then solve for the best-fitting distribution of slip in a least-squares sense, using the elastic dislocation model of Okada [1985]. We use a fixed fault geometry based on the strike, dip and rake of our single-fault seismic model (strike 357° , dip 88° , rake -166° , Auxiliary Figure 2), with a length of 20 km, a width of 16 km, divided into 80, 2×2 km patches, and surfacing at the observed surface rupture. We apply Laplacian smoothing between patches in order to prevent unphysical oscillatory slip [Jónsson *et al.*, 2002]. The model result (Auxiliary Figure 4a) does not successfully match the deformation south of Bam, resulting in a large unmodeled phase residual (Auxiliary Figure 4b).

The fit to the data can be improved if a second, thrust fault, as required by the seismology, is included. Again, we adopt the strike, dip and rake of the seismic solution for this second fault (strike 180° , dip 30° , rake 90° , Auxiliary Figure 2). We then solve for its location and depth range, using a downhill simplex algorithm with multiple Monte-Carlo restarts [Wright *et al.*, 1999]. Using a down-dip width for the thrust of 10 km, a fault length of 16 km, and dividing the fault plane into 64 2×1.1 km patches, we solve simultaneously for the slip on both this and the strike-slip fault. The result (Auxiliary Figure 4c) is a closer match to the observed pattern of deformation, with the remaining residuals

(Auxiliary Figure 4d) mostly being of short wavelength, and therefore likely to be the result of unmodeled fault complexity. Our model fault locations are given in Auxiliary Table 1.

To estimate the uncertainty in our calculated fault slip distribution (Auxiliary Figure 5a) we use a Monte Carlo estimation method, using realistic correlated noise [e.g. *Wright et al.*, 2003]. The statistical properties of far-field spatially-correlated noise in the interferogram are used to generate 100 perturbed displacement datasets through the addition of randomly-generated noise with the same degree of correlation. These datasets are then inverted as above to give 100 model slip estimates for each patch on the fault. The standard deviations of each patch (estimated 1σ uncertainties) are plotted in Auxiliary Figure 5b. Uncertainty is greatest at depths greater than 10 km on the fault, where the 1σ values reach 0.3 m, and at the surface within the decorrelated area of Bam, at the northern end of the fault.

References

- Jónsson, S., H. Zebker, P. Segall, and F. Amelung, Fault slip distribution of the 1999 Mw 7.1 Hector Mine earthquake, California, estimated from satellite radar and GPS measurements, *Bull. Seismol. Soc. Am.*, *92*, 1,377–1,389, 2002.
- Massonnet, D., and K. L. Feigl, Radar interferometry and its application to changes in the earth's surface, *Rev. Geophys.*, *36*(4), 441–500, 1998.
- McCaffrey, R., and G. Abers, *SYN3: A program for inversion of teleseismic body waveforms on microcomputers*, Air Force Geophysical Laboratory, Hanscomb Air Force Base, Massachusetts, 1988.

- McCaffrey, R., P. Zwick, and G. Abers, Syn4 program, *IASPEI Software Library*, 3, 81–166, 1991.
- Okada, Y., Surface deformation due to shear and tensile faults in a half-space, *Bull. Seismol. Soc. Am.*, 75, 1,135–1,154, 1985.
- Rosen, P. A., S. Hensley, I. R. Joughin, F. K. Li, S. N. Madsen, E. Rodriguez, and R. M. Goldstein, Synthetic aperture radar interferometry, *Proceedings of the IEEE*, 88, 333–382, 2000.
- Rosen, P. A., S. Hensley, G. Peltzer, and M. Simons, Updated Repeat Orbit Interferometry package released, *Eos Trans. AGU*, 85, 35, 2004.
- Wessel, P., and W. H. F. Smith, New, improved version of generic mapping tools released, *Eos Trans. AGU*, 79, 579, 1998.
- Wright, T. J., B. Parsons, J. Jackson, M. Haynes, E. Fielding, P. England, and P. Clarke, Source parameters of the 1 October 1995 Dinar (Turkey) earthquake from SAR interferometry and seismic bodywave modelling, *Earth Planet. Sci. Lett.*, 172, 23–37, 1999.
- Wright, T. J., Z. Lu, and C. Wicks, Source model for the M_w 6.7, 23 October 2002, Nenana Mountain Earthquake (Alaska) from InSAR, *Geophys. Res. Lett.*, 30, doi:10.1029/2003GL018,014, 2003.
- Zwick, P., R. McCaffrey, and G. Abers, Mt5 program, *IASPEI Software Library*, 4, 1994.

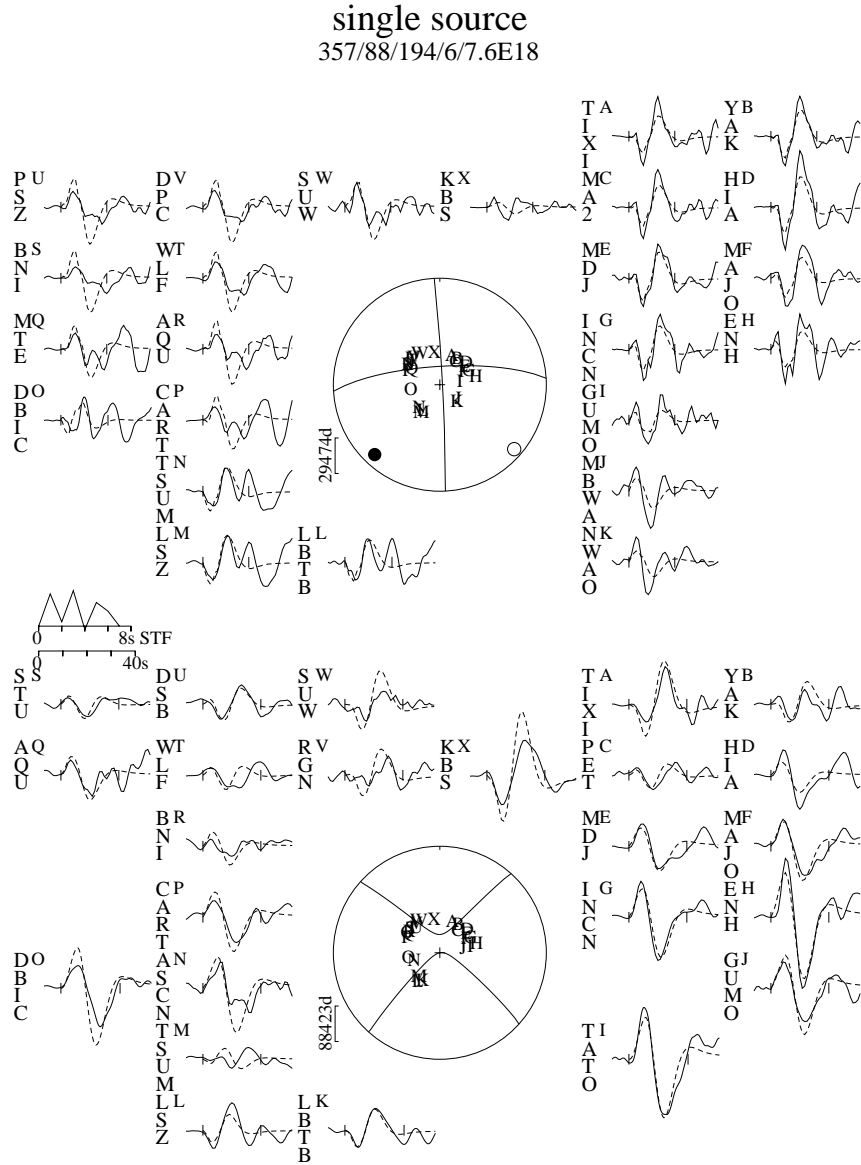


Figure 1. Auxiliary Figure 1: P (top) and SH (bottom) synthetic (dashed) and observed (solid) waveforms for a single source mechanism for the Bam mainshock. The source parameters of the source mechanism used are under the header and indicate the strike, dip, rake, centroid depth and seismic moment (in Nm). Capital letters next to the station codes correspond to their position on the focal sphere, which are ordered clockwise by azimuth, starting at north. The solid lines on the focal sphere show the nodal planes. The inversion window is marked by vertical lines on each waveform. The source time function (STF) is shown, along with the time scale for the waveforms and the relative amplitude scales for the waveforms. The P and T axes are shown by the solid and open circles respectively. Synthetic waveforms were calculated in a half-space with V_p 6.5 km s^{-1} .

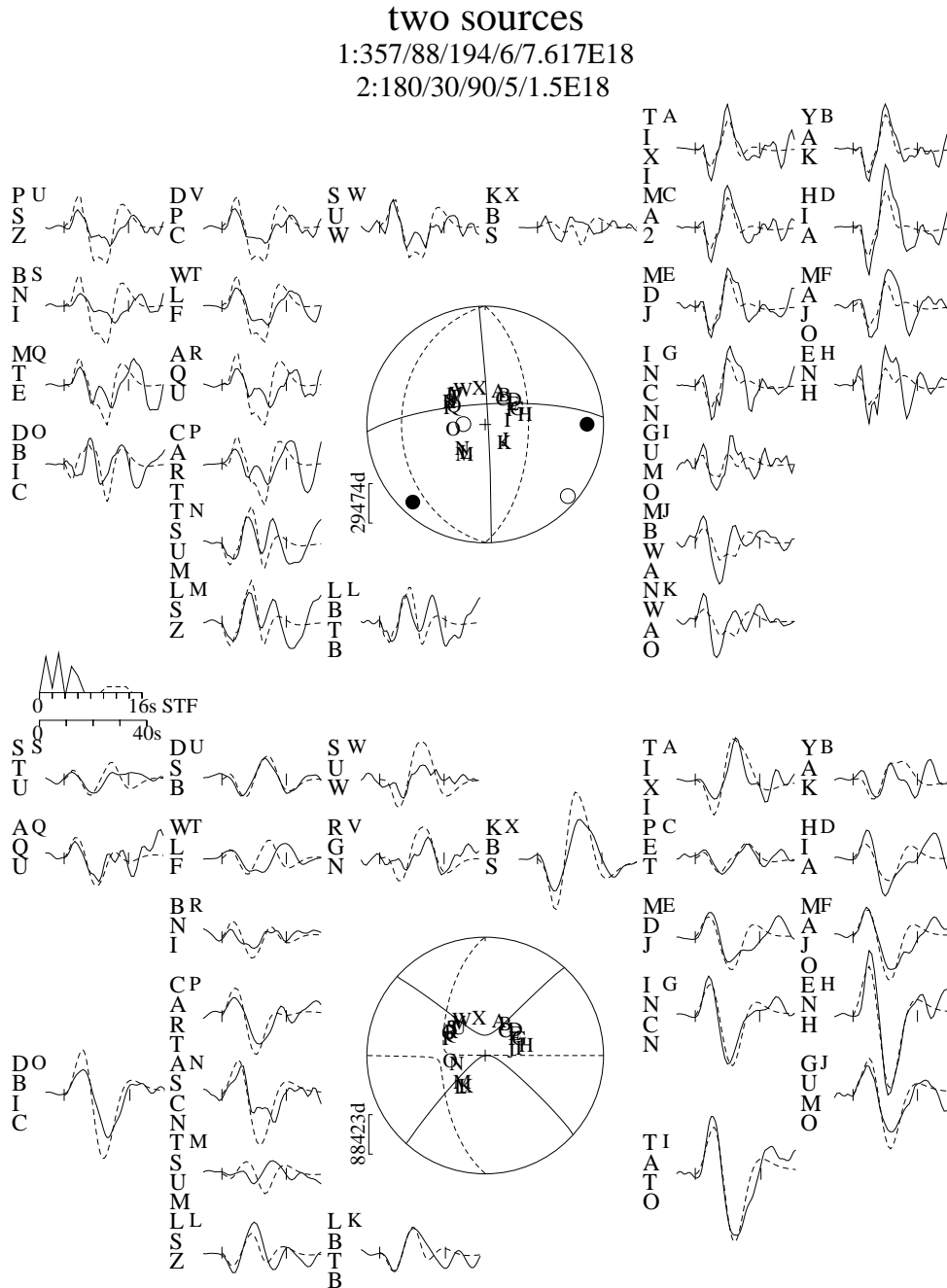


Figure 2. Auxiliary Figure 2: P (top) and SH (bottom) synthetic (dashed) and observed (solid) waveforms for a two source mechanism for the Bam mainshock. As for Auxiliary Figure 1, except that the dashed lines on the focal sphere show the nodal planes for the second sub-event as well, and the dashed lines on the source time function are also for the second sub-event.

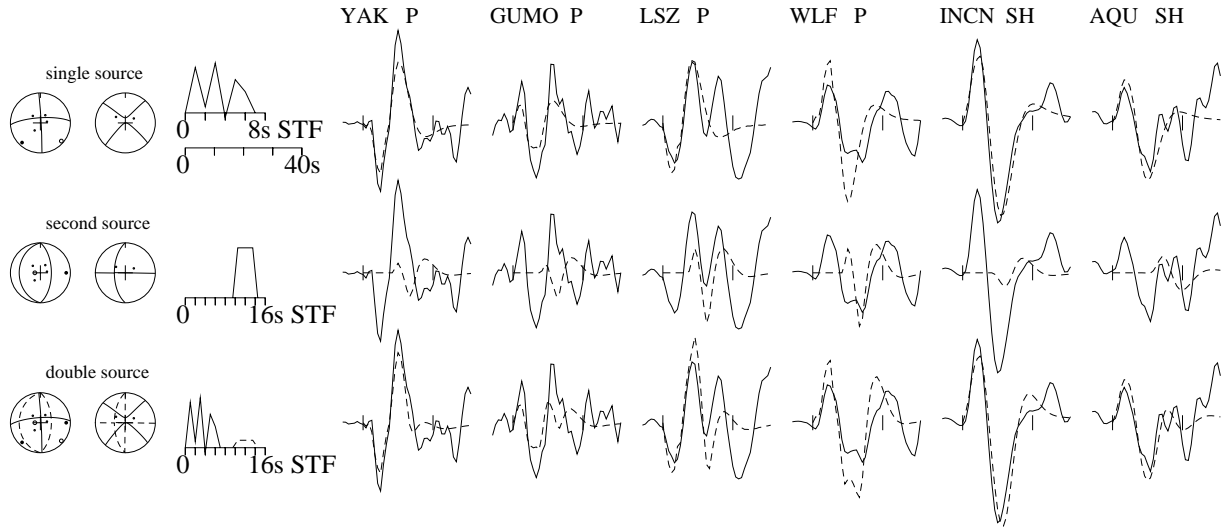


Figure 3. Auxiliary Figure 3: Figure to show the contribution of the smaller, second sub-event to the synthetic seismograms. Synthetic seismograms are dashed, observed are solid lines. The first line contains selected stations and seismograms with synthetics calculated for the first source only. P and SH focal spheres are shown, with the time function. Vertical bars are 25 seconds apart. Note the clear down pulse 13 s after the onset at LSZ and up pulse at 10 s at WLF in the observed seismograms. The second line shows the contribution of the minor thrust sub-event, which produces appropriate pulses at LSZ and WLF, but smaller effects at other azimuths and for SH. The third line shows seismograms for the two-source source solution, made by adding lines 1 and 2 together.

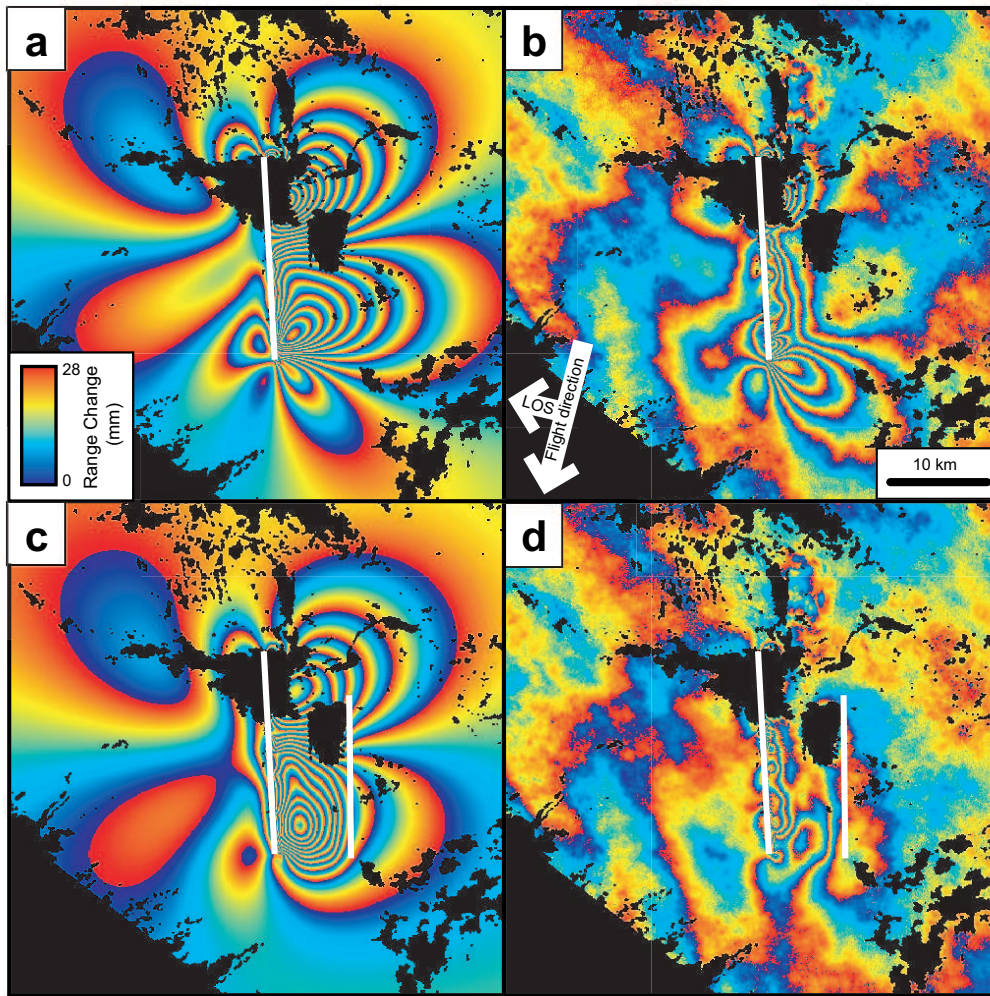


Figure 4. Auxiliary Figure 4: (a) Synthetic interferogram generated using our single-fault, distributed slip model; (b) Residuals to model shown in (a); (c) Synthetic interferogram for two-fault, distributed slip model; (d) Residuals to model shown in (c). White lines are the surface projections of the model fault planes. Areas as for Figure 3a.

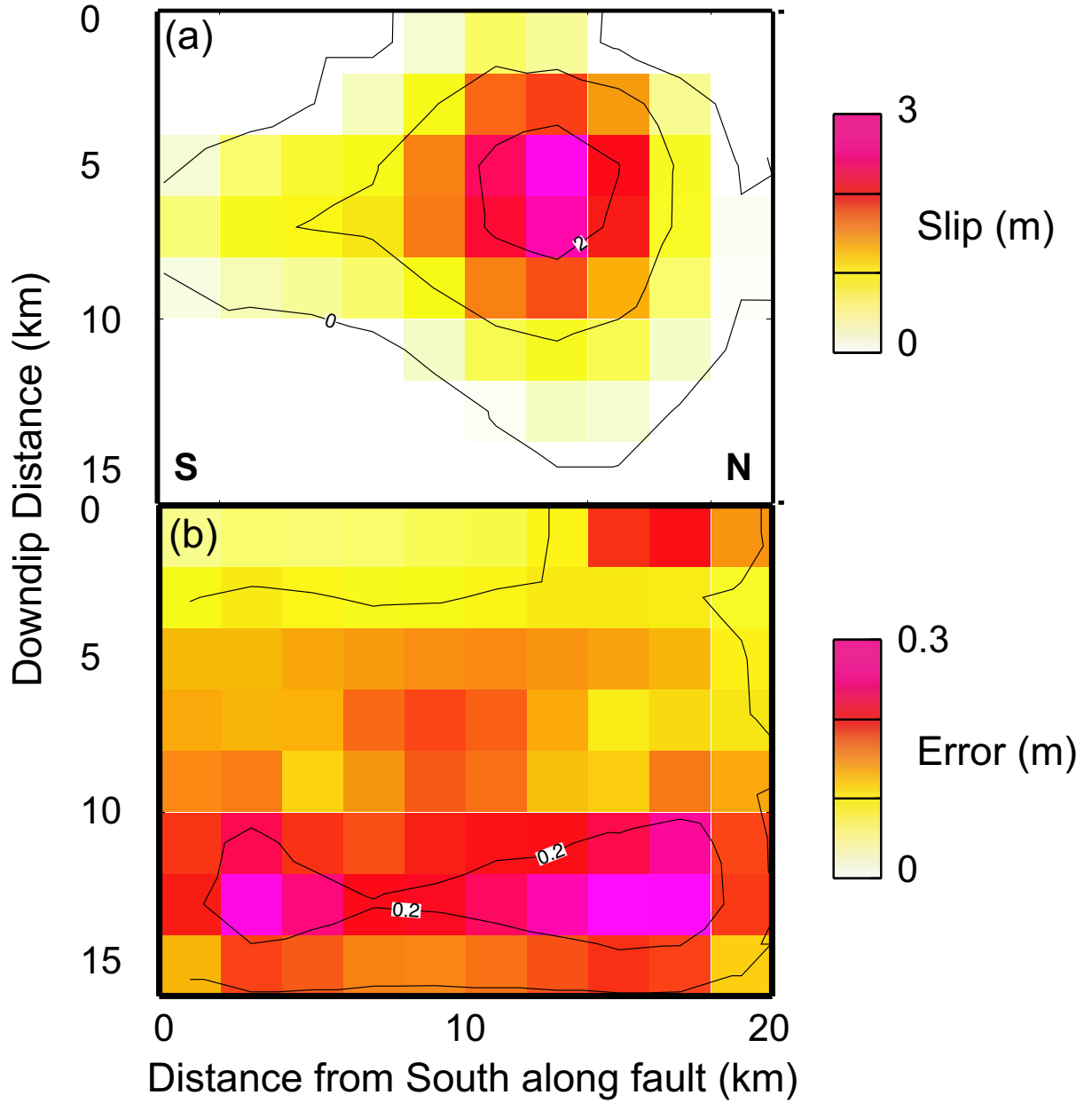


Figure 5. Auxiliary Figure 5: (a) Distribution of slip on the main, strike-slip fault.(b) 1σ uncertainties for values of slip, calculated by Monte Carlo analysis using realistic noise [e.g. *Wright et al.*, 2003, see auxiliary text for further details].

Table 1. Auxiliary Table 1: Fault parameters for the InSAR two-fault distributed slip model.

	Strike	Dip	Rake	M_0/Nm^{a}	Easting ^b	Northing ^b
Main fault	357°	88°	-166°	5.8×10^{18}	58.362°	29.052°
Secondary fault	180°	30°	90°	1.3×10^{18}	58.443°	29.029°

^a Using shear modulus, $\mu = 3.43 \times 10^{10}$ Nm.

^b Location of the centre of the line of intersection between the fault plane and the surface.